MTLA 33 (2024) 101989

Contents lists available at ScienceDirect

Materialia

journal homepage: www.elsevier.com/locate/mtla

Full length article

Mean-field modeling and Phase-field simulation of Grain Growth under Directional driving forces

Vitaliy M. Kindrachuk *, Reza Darvishi Kamachali *

Federal Institute for Materials Research and Testing (BAM), Unter den Eichen 87, 12205 Berlin, Germany

ARTICLE INFO

Keywords:
Directional grain growth
Mean-field modeling
Phase-field simulation
Microstructure evolution
Additive manufacturing

ABSTRACT

Directional grain growth is a common phenomenon in the synthetic and natural evolution of various polycrystals. It occurs in the presence of an external driving force, such as a temperature gradient, along which grains show a preferred, yet competitive, growth. Novel additive manufacturing processes, with intense, localized energy deposition, are prominent examples of when directional grain growth can occur, beneath the melting pool. In this work, we derive a phenomenological mean-field model and perform 3D phase-field simulations to investigate the directional grain growth and its underlying physical mechanisms. The effect of the intensity of driving force is simulated and systematically analyzed at the evolving growth front as well as various cross-sections perpendicular to the direction of the driving force. We found that although the directional growth significantly deviates from normal grain growth, it is still governed by a power law relation $\langle R\rangle \propto t^n$, with an exponent $n \sim 0.6$–0.7. The exponent n exhibits a nontrivial dependence on the magnitude of the directional driving force, such that the lowest growth exponent is observed for intermediate driving forces. We elaborate that this can originate from the fact that the forces at grain boundary junctions evolve out of balance under the influence of the directional driving force. With increasing the driving forces, the growth exponent asymptotically approaches a value of $n \approx 0.63$, imposed by the largest possible grain aspect ratio for given grain boundary energies. The current combined mean-field and phase-field framework pave the way for future exploration in broader contexts such as the evolution of complex additively manufactured microstructures.

1. Introduction

Grain growth has a significant impact on the thermal stability and safety of processing and performance in polycrystalline materials. This is a pervasive phenomenon happening in almost all kinds of artificially synthesized and naturally occurring polycrystalline including metallic materials [1,2], ceramics [3,4], polymers [5], and composites [6] as well as biominerals such as bivalve shells [7] and hydroxyapatite bones [8]. Extensive studies conducted on normal grain growth mainly assume isotropic conditions of grain growth/shrinkage with no external effects. However, most real-world polycrystalline materials evolve under complex manufacturing processes or natural conditions that impose certain driving forces, e.g., temperature gradients, leading to directional grain growth (DGG). In certain occasions, it is actually desired to achieve a DGG, such as in the fabrication of some functional materials under an external field [9], producing columnar-grained structures in thin films [10] or via directional annealing [11]. DGG is also commonly observed and studied in naturally occurring polycrystals such as the mollusc bivalve shell Pinna nobilis [12].

With the emergence of novel additive manufacturing (AM) techniques, the significance of the DGG phenomenon needs to be revisited. In fact, the unavoidable application of directional heat during the non-equilibrium AM processes is found to greatly influence the evolution of microstructure beneath the melting pool [14–16]. Fig. 1 demonstrates the massive change in the grain size along the building direction in an AMed AlScZr alloy, due to the intrinsic directional heating [13]. To control the directionally evolving microstructures, it is critical to learn about the kinetics of DGG. Yet, despite its significance and broad appearance in various applications, our current understanding of DGG remains elusive so far. It is indeed unclear, how the corresponding grain size and shape distributions may depend on the additional (directional) driving forces? And whether the principles of self-similar grain growth can hold for DGG? As the experimental measurement of directionally evolved polycrystals is quite challenging, modeling and simulation can greatly assist. To answer the above questions is a two-fold task, first to develop a theoretical framework incorporating such directional

* Corresponding authors.
E-mail addresses: vitaliy.kindrachuk@bam.de (V.M. Kindrachuk), reza.kamachali@bam.de (R. Darvishi Kamachali).

https://doi.org/10.1016/j.mtla.2023.101989
Received 8 August 2023; Accepted 7 December 2023
Available online 20 December 2023

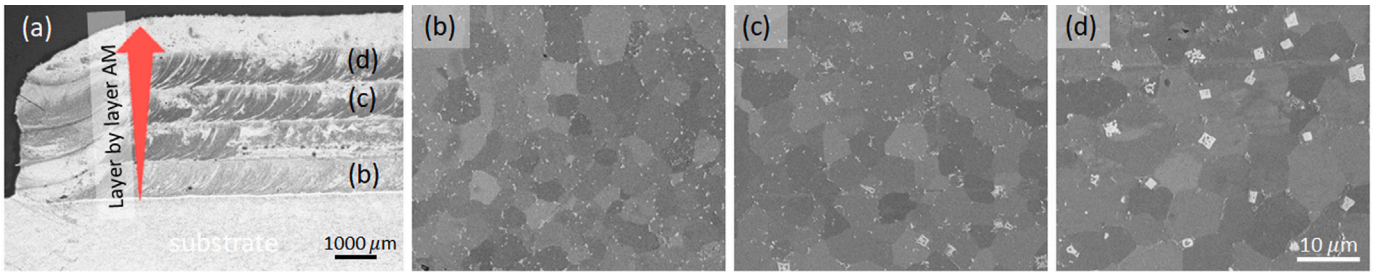

Fig. 1. Grains evolution upon intrinsic heating during the AM of an AlScZr alloy. The material is exposed to intense directional temperature gradients along the building direction. The AMed specimen is shown in a cross-section view (a), with SEM micrographs showing the grain size differences in three layers (b), (c) and (d) along the building direction. Reconstructed with permission from [13].

driving forces and, second, to establish a computational framework for examining the parameters of DGG, systematically.

Laid on robust physical principles and a measurable set of variables, mean-field modeling has proven to be a powerful tool for understanding microstructure evolution. The mean-field theory of grain growth has been the subject of early works by Hillert [17], Brown [18], Coughlan and Fortes [19] and Rios [20] as well as many recent works [21–25]. In these models, grain growth is described in terms of the average curvature of each grain, governing its temporal evolution while maintaining the conservation and continuity in the system. The average curvature concept has this drawback that neglects grains' geometrical aspects and the interconnectivity of grain boundaries throughout the system. The multi-phase-field (MPF) simulation has emerged as a powerful tool capable of capturing the grains' geometrical aspects and the grain boundaries' network, in a thermodynamically consistent manner. MPF has been successfully applied for studying precipitation [26–30], recrystallization [31], effect of micro-elasticity [32] as well as surface and junction diffusion phenomena [33]. Quantitative application of MPF modeling to grain size distribution [34], microstructure evolution in additively manufactured Inconel 718 [35] and directional eutectic melting [36] are also demonstrated.

In a series of previous studies, we have shown that mean-field modeling and phase-field simulations can be efficiently coupled for studying grain growth in polycrystalline materials [37–39]. The directionality of the external driving force shifts the balance between grains in a complex manner, strongly coupled to the arrangement of grains and grain boundaries' network. In fact, previous research shows that the application of classical mean-field models cannot resolve the essence of a DGG [12]. In this work, we revisit the mean-field theory of normal grain growth and propose a modified model for studying DGG. We then perform systematic MPF simulations to capture the underlying physics. The results of MPF simulations are then analyzed in the context of the extended mean-field model. We discuss the mechanisms of DGG in light of modeling and simulation results and with a geometrical consideration of evolving grains.

In the following, we first present a phenomenological modification of the mean-field model for DGG. The MPF model and related simulation procedures are given in Section 3. In Section 4, we present the results of our MPF simulations and compare the effect of the external driving force (its magnitude) on the kinetics of DGG and the morphology of the grains. A detailed discussion of our results and the implications of our findings are presented in Section 5.

2. Modified mean-field model for directional grain growth

To address DGG, we expand our previous derivations and analysis of normal grain growth [39] by considering a generalized equation of growth:

$$\frac{dR}{dt} = \alpha M\sigma\left(\frac{1}{R_{cr}} - \frac{1}{R}\right)\cdot\frac{1}{R^{\beta}} \tag{1}$$

with R the radius of a given grain, M the GB mobility, σ the GB energy, R_{cr} the critical radius (of the grains' population in the given polycrystalline body) and α being a geometrical coefficient. Here, the multiplicative term $\frac{1}{R^{\beta}}$, with the additional model parameter β, accounts for any external driving forces that can interfere with the normal curvature-driven evolution, leading to DGG. A different empirical extension of the mean-field model was recently used by [40], considering the pinning effect of the precipitated particles on the growing grains.

For an external driving force applied as a field, a negative β value is expected, indicating that the driving force is received by each existing grain proportional to its size. This formulation implies a reasonable generality, such that, an external driving force can modify the curvature effect as well as the scaling of the growth rate. Note that here α is a dimensionless coefficient only when $\beta = 0$, for which we recover Hillert's rate equation [17] and thus the results in our previous study [39]. With $\beta = 1$, Eq. (1) becomes the Lifshitz–Slyozov rate equation for precipitates' ripening [41].

Introducing the relative grain size $\rho = \frac{R}{R_{cr}}$ and a new timescale $\tau = \ln R_{cr}^{(2+\beta)}$ we obtain

$$\frac{d\rho^{2+\beta}}{d\tau} = \gamma(\rho - 1) - \rho^{2+\beta}, \tag{2}$$

$$\gamma = (2+\beta)\alpha M\sigma\frac{dt}{dR_{cr}^{2+\beta}}. \tag{3}$$

Eq. (2) can be rewritten as

$$\frac{d\rho}{d\tau} = \dot{\rho} = \frac{\gamma(\rho-1) - \rho^{2+\beta}}{(2+\beta)\rho^{1+\beta}}. \tag{4}$$

In what follows, the dot derivative denotes the derivative with respect to τ. Eqs. (2)–(4) assume that R_{cr} grows monotonically with time as

$$R_{cr}^{2+\beta}(t) - R_{cr}^{2+\beta}(t_0) = Kt \tag{5}$$

with the growth coefficient $K = (2+\beta)\gamma^{-1}\alpha M\sigma$, and $t_0 = 0$ being the initial time.

Similar to the normal grain growth [39], the physical solutions for the DGG shall be obtained when the rate $\dot{\rho}$ remains negative. Considering this and a special case that $\dot{\rho}$ has a single root (ρ_0), with $\dot{\rho} = 0$ and $\frac{d\dot{\rho}}{d\rho} = 0$, gives the system of equations

$$\gamma - (2+\beta)\rho^{1+\beta} = 0, \tag{6}$$

$$\gamma(\rho-1) - \rho^{2+\beta} \le 0. \tag{7}$$

Eqs. (6) and (7) are valid for $\beta > -2$. Solving these equations results in inequalities

$$\rho \le \rho_0 = \frac{2+\beta}{1+\beta}, \tag{8}$$

$$\gamma \le \gamma_0 = \frac{(2+\beta)^{2+\beta}}{(1+\beta)^{1+\beta}}. \tag{9}$$

Here ρ_0 is the maximum achievable grain size corresponding to the mean-field coefficient γ_0, obtained when the growth rate is assumed

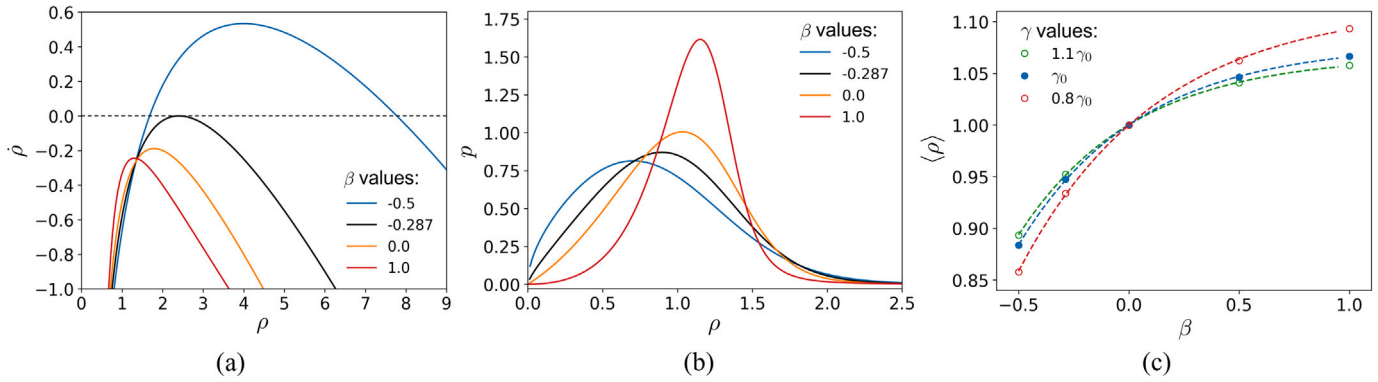

Fig. 2. (a) Growth rate Eq. (4) plotted for $\gamma = 3.2 = 0.8\gamma_0$, which corresponds to the reference solution from [39]. For $\beta = -0.287$ the first single root is found. (b) Relative grain size distribution, Eq. (17), computed for the various values of the exponent β for $\gamma = 3.2$. (c) Average grain size $\langle\rho\rangle$ is shown as a function of β. The distributions for higher values of γ are provided in Fig. S1 in the Supplementary Material (SM).

to have a single root. In the vicinity of $\gamma_0 = \frac{(2+\beta)^{2+\beta}}{(1+\beta)^{1+\beta}}$, the kinetic Eq. (5) is given by $K = K_0 = \left(\frac{1+\beta}{2+\beta}\right)^{1+\beta} \alpha M \sigma$.

In the case of normal grain growth ($\beta = 0$), Eqs. (8) and (9) give *limiting regime* of $\gamma_0 = 4$ with $\rho_0 = 2$. However, we have previously shown that valid solutions for normal grain growth ($\beta = 0$) are obtained for $\gamma \approx 3.2$ [39], different from this limiting regime.

For normal grain growth with $\gamma \approx 3.2$, which is our reference verified case, the growth rate $\dot{\rho}$ was shown to be always negative with no root. But in the presence of an external driving force, with $\beta \neq 0$, much more complex situations can emerge: Fig. 2a shows $\dot{\rho}$ for $\gamma = 3.2$ and various β values. The plot shows that the value of β, representing the intensity of the external driving force, can have a significant impact on the growth rate, which increases and eventually gets positive values when $\beta \leq -0.287$. This means that the external driving force tends to narrow the range of relative grain size. Interestingly, we find that by varying the β values, the growth rate in a certain range of grain size increases while it decreases in the rest (Fig. 2a).

For arbitrary β and γ values, the analytical solutions for the roots of $\dot{\rho}$ are impractical to write down. Nevertheless, one can show that there can be up to two roots, as demonstrated in Fig. 2a. We note that the variation in the range of grain size and corresponding β and γ does not disturb the power-law dependency of $R_{cr} \sim t^{1/(2+\beta)}$ in Eq. (5) that holds through the whole range of inequality (9).

2.1. Grain size distribution

Considering the number of grains in the interval between ρ and $\rho + d\rho$ as $\Phi(\rho, \tau)d\rho$, from the continuity in the grain-size space we can write

$$\frac{\partial \Phi}{\partial \tau} + \frac{\partial}{\partial \rho}(\dot{\rho}\Phi) = 0\,. \tag{10}$$

Assuming a multiplicative decomposition, $\Phi(\rho, \tau) = N(\tau)P(\rho)$, with N the number of grains and P the probability function (size distribution), leads to the system of equations

$$\frac{1}{N}\frac{\partial N}{\partial \tau} = -C, \tag{11}$$

$$\frac{1}{P}\frac{\partial}{\partial \rho}(P\dot{\rho}) = C, \tag{12}$$

where C is a positive constant. Eq. (11) implies an exponential decay $N(\tau) = N_0 \exp(-C\tau)$. Considering the conservation of the total area (volume) of the grains in 2D (3D), the term $R^d N(\tau) = \rho^d R_{cr}^d N(\tau)$ must be independent on time τ. Here $d = 2$ and $d = 3$ for 2D and 3D situations, respectively.

For studying DGG, grains' evolution in a 2D cross-section/surface, perpendicular to the direction of the driving force, is of interest. Using $R_{cr} = \exp(\frac{\tau}{2+\beta})$, we find that $N(\tau)\exp\left(\frac{2\tau}{2+\beta}\right) = const$ must hold for the 2D case, which gives

$$N(\tau) = N_0 \exp\left(\frac{-2\tau}{2+\beta}\right), \tag{13}$$

and thus $C = \frac{2}{2+\beta}$.

In order to obtain the grain size distribution, we follow our previous considerations [39], choosing $h(W(\rho)) = P(\rho)\dot{\rho}$, Eq. (12) converts to

$$\left(\frac{1}{h}\frac{d\,h}{d\,W}\right)\left(\dot{\rho}\frac{d\,W}{d\,\rho}\right) = \frac{2}{2+\beta}. \tag{14}$$

The first product term is a function of W and the second one only depends on ρ. Because of this multiplicative decomposition of variables, the equation can be fulfilled only if each product term is a constant. That ultimately gives

$$W(\rho) = \int_0^{\rho} \frac{1}{\dot{\rho}}\, d\rho\,, \tag{15}$$

whereas $h(W) = h_0 \exp\left(\frac{2W}{2+\beta}\right)$, and, the size distribution function is directly related by definition to $h(W(\rho))$, that is $P(\rho) = \frac{h_0}{\dot{\rho}} \exp\left(\frac{2W(\rho)}{2+\beta}\right)$, which must satisfy

$$\int_0^{\rho^{max}} P(\rho)\, d\rho = \frac{h_0(2+\beta)}{2}\int_0^{-\infty} \frac{1}{\dot{\rho}}\frac{d\,\rho}{d\,W}\, d\exp\left(\frac{2W}{2+\beta}\right) = 1. \tag{16}$$

Using this condition and Eq. (15), we get for $h_0 = -\frac{2}{2+\beta}$, and the size distribution function as

$$P(\rho) = -\frac{2\rho^{1+\beta}}{\gamma(\rho-1) - \rho^{2+\beta}}\, \exp\left(\frac{2W(\rho)}{2+\beta}\right). \tag{17}$$

The valid solutions for the size distribution are obtained when $W(\rho)$ gives a negative value, which is shown to be possible up to the first root of $\dot{\rho}$ [39].

The distribution function, Eq. (17), is plotted in Fig. 2b. The results show that the grain size distribution is sensitive to the exponent β, i.e., the driving force. Note that the distribution function bounds the possible grain sizes in accordance with Eq. (8), that is, in the asymptotic limit, when γ approaches γ_0 in Eq. (9). The most interesting solutions, however, occur when $\gamma < \gamma_0$: In this case, even though we see that the probability function almost vanishes for $\rho > \rho_0$, it is still defined on the whole interval $[0, +\infty)$, as $W(\rho)$ is negative and integrable.

For 2D case, the critical grain size and the average relative grain size can be respectively obtained as

$$R_{cr} = \frac{\langle R^{1-\beta}\rangle}{\langle R^{-\beta}\rangle}, \tag{18}$$

and

$$\langle \rho \rangle = \frac{\langle R \rangle}{R_{cr}} = \int_0^{\rho^{max}} \rho \; P(\rho) \; d\rho. \tag{19}$$

Here $\langle x \rangle = \frac{1}{N(\tau)} \sum_i^{N(\tau)} x_i$ and the integral is given over the entire valid range of ρ. The average relative grain size $\langle \rho \rangle$ is very practical for the purpose of investigating the growth phenomenon. Following the grain size distributions in Fig. 2b, we find that the average relative grain size increases for $\gamma < \gamma_0$, shown in Fig. 2c. We find that for $\beta < 0$, the average relative grain size decreases with decreasing the γ value.

The central focus of our study will be concerning the growth exponent n in $\langle R \rangle \propto t^n$ and its dependence on the driving forces in the DGG process. Considering Eqs. (5) and (19) we obtain the average grain size as

$$\langle R \rangle \propto \left[\frac{2+\beta}{\gamma} \right]^n \langle \rho \rangle \, (\alpha M \sigma t)^n \, . \tag{20}$$

with $n = \frac{1}{2+\beta}$, giving the temporal evolution of average grain size in the presence of an external driving force. Again, assuming that $\langle \rho \rangle \to 1$ and $\beta \to 0$, Eq. (20) simplifies to normal grain growth kinetics [39].

3. MPF simulations

In a polycrystalline body, the interfacial energy density in the MPF framework reads [42]:

$$f^{intf} = \sum_{i,j,i \neq j} \frac{4\sigma_{ij}}{\eta} \left(\phi_i \phi_j - \frac{\eta^2}{\pi^2} \nabla \phi_j \cdot \nabla \phi_j \right) + \frac{8}{\pi} \sum_{i,j,i \neq j} h_0 \left(\phi_i, \phi_j \right) \Delta g_{ij}, \tag{21}$$

in which the sums run over all possible (dissimilar) pairs of N present grains. The phase-field variable $\phi_i(\vec{x}, t) \in [0, 1]$ defines the presence of the grain i with the constraint $\sum_i^N \phi_i = 1$ in every point of space and time. η is the width and σ_{ij} is the energy of the grain boundary between grains i and j. The energy term Δg_{ij} accounts for any additional driving force applied on the grain boundary. For our DGG simulations, $\Delta g_{ij} = \Delta g$ is taken to be a spatially uniform, linear energy field favoring grains to grow along the z-axis. More precisely, $\Delta g = \delta g \; (z/\ell) \boldsymbol{e}_z$ is considered, as a vector field, with $\boldsymbol{e}_z$ the unity vector along the z-axis and ℓ the grid spacing. Similar (directional) evolution of grains in thin films were simulated by other methods but without interaction with an external field [10]. For convenience, the direction of the energy field is denoted on the respective figures. Here h_0 is a pairwise function to distribute the driving force over each grain boundary. The intensity of δg is later discussed as a simulation parameter.

With $F = \int f^{intf} \; dV$ and considering isotropic grain boundary energy ($\sigma_{ij} = \sigma$) and mobility ($M_{ij} = M$), the temporal evolution of the phase-fields follow

$$\begin{aligned} \dot{\phi}_i &= -\frac{\pi^2 M}{8\eta N} \sum_{j=1}^{N} \left(\frac{\delta F}{\delta \phi_i} - \frac{\delta F}{\delta \phi_j} \right) \\ &= M\sigma \sum_{j=1}^{N} \left(\nabla^2 \phi_i - \nabla^2 \phi_j + \frac{\pi^2}{2\eta^2} (\phi_i - \phi_j) \right) \\ &+ M \frac{\pi}{\eta} \sum_{j=1}^{N} h \left(\phi_i, \phi_j \right) \Delta g, \end{aligned} \tag{22}$$

where we use $h = \frac{\partial h_0}{\partial \phi_j} = \sqrt{\phi_i \phi_j}$ as the distribution function, the integral of which, over a flat grain boundary, is equal to 1. Using this function allows for obtaining a uniform driving force within the grain boundary region [37]. The simulations were performed using OpenPhase software package [30,37,43]. For an efficient calculation, we have implemented a dynamic memory allocation procedure, in which we only trace and store the phase-fields with values between 0 and 1. This procedure is constructed using the list function in C++ which allows the addition and removal of members. The phase-fields are stored in a paired structure including the grain index and its phase-field value. These are then pushed back or removed to/from the C++ list, based on their creation/vanish in every given point of space and time step. This approach significantly reduces computational costs by reducing the computational domain to the grain boundary region. Further details on the OpenPhase implementations can be found in [37].

Table 1
Material parameters and input values for the numerical studies.

Parameter	Values	Dimension
M, grain boundary mobility	3×10^{-9}	$m^4\ J^{-1}\ s^{-1}$
σ, grain boundary energy	0.17	$J\ m^{-2}$
η, grain boundary width	5ℓ	m
ℓ, grid spacing	1×10^{-6}	m
Δt, time increment	5×10^{-5}	s
δg, intensity of external energy field	1 to 10	$MJ\ m^{-3}$

3.1. Simulation setup

Series of MPF simulations were performed in which small seeded grains grow, directionally, under the uniaxial driving force Δg of various intensities. The Δg is applied along the z-axis, thus dictating the DGG in this direction. The simulation domain is discretized using a regular grid spacing $\Delta x = \Delta y = \Delta z = \ell = 1$ μm and a constant time step $\Delta t = 5 \cdot 10^{-5}$ s. We study a simulation box of size $450\ell \times 450\ell \times 205\ell$, Fig. 3a. We note that these dimensions give us a fairly large domain compared to the previous studies [37] yet somewhat limited for studying DGG, as we discuss in the following. Each phase-field represents an individual grain, with grain boundaries shown as gray curves in the figure. Periodic boundary conditions were applied along the x- and y-axis and a zero gradient boundary condition $\nabla \phi_i = \mathbf{0}$ along z axis.

The initial grain configuration plays a crucial role in DGG. This is due to the non-equilibrium nature of the process, during which a random initialization could achieve a steady state only after an extended period. In terms of simulation, this then requires a significantly large representative volume beyond available computational capacities. Hence, a more controlled initialization is considered here, mimicking the later stage of the DGG process. Initial grains were seeded on a checkered pattern of 45 by 45 (2025 grains in total), each with finite random variations in its size ($R_0 = 5\ell \pm 20\%$) and position ($\pm 0.1 R_0$ applied for both x and y coordinates), respectively. Figure S2 (left) in the SM demonstrates the initial configuration. This initialization is further referred to as Initial Grain Distribution IGD1. Additionally, we considered an almost ideal initial grain distribution (IGD2) with the initial size varying as $R_0 = 5\ell \pm 5\%$ and the uncertainty in position is bounded by $\pm 0.05 R_0$. The IGD2 pattern is less disturbed and more stable in the context of grains' competitions throughout MPF simulations, here studied for the sake of comparison with the IGD1. Related simulation parameters are listed in Table 1.

3.2. Concept of moving box

Detailed investigation of DGG requires large-scale simulation domains, especially with extended dimensions along the direction of the driving force, which is necessary to establish a steady DGG evolution. In order to achieve this, we performed additional MPF simulations using a moving frame, such that the much smaller, and therefore computationally cheaper, simulation domain shifts and follows the vicinity of the evolving front during the DGG. The idea behind the concept of the moving box resembles the Scheil box used for the simulation of the solidification problems [44], — that is moving through the microstructure as the solidification occurs and the temperature drops.

Due to the gradient energy contributions, Eq. (22), and the non-local effects arising from the connected grain boundaries' network, the

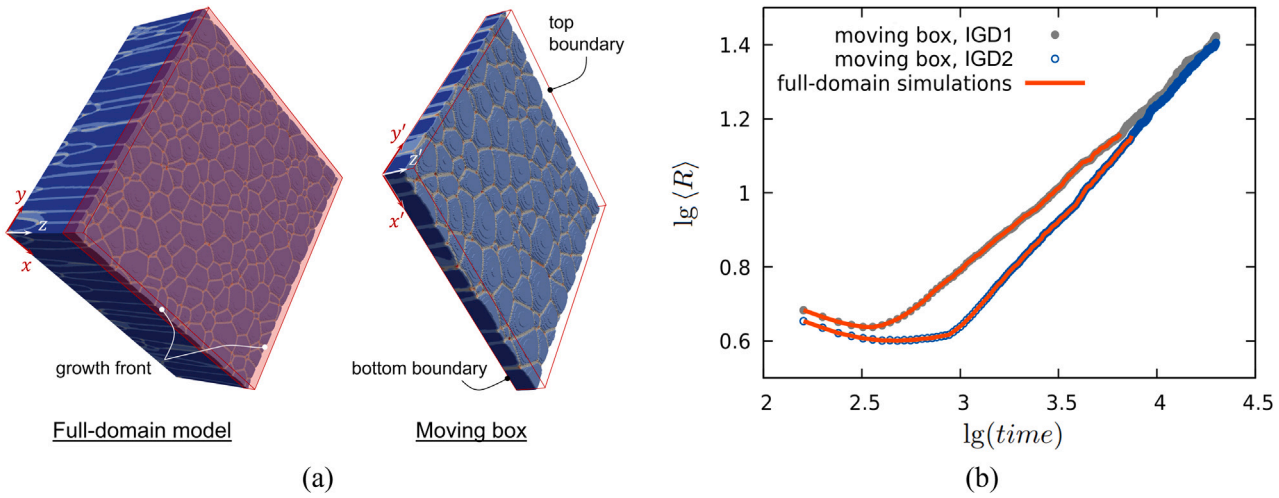

Fig. 3. (a) Full-domain simulation (on the left) with grains growing parallel to the external force, that is along the z-axis. The grain boundaries are shown in gray and the junctions are in orange. The empty volume of the box is occupied by the parent phase. Following the concept of the moving box, the full-domain simulation can be replaced by a simulation within the red box. The respective simulation box is depicted on the right. Here the boundary conditions on the bottom boundary are updated at each succeeding time increment. (b) Evolution of the mean variable $\langle R \rangle$ evaluated on the evolving front. Both, the full-domain simulations and the reduced simulations due to the moving-box concept, produce almost identical results. The applied intensity of the energy field was 2.4 MJ m^{-3}. (For interpretation of the references to color in this figure legend, the reader is referred to the web version of this article.)

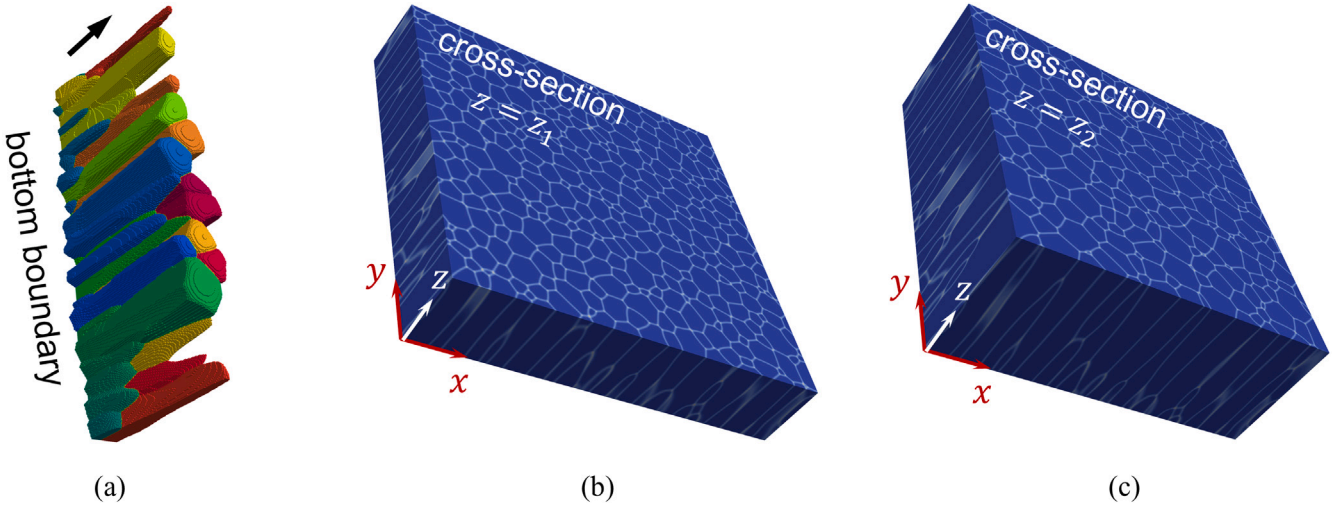

Fig. 4. Selected grains (a) are depicted together with the cross-sections of the simulation domain at $z = z_1$ (b) and $z = z_2 > z_1$ (c). The black arrow shows the growth direction, which coincides with the direction of the z-axis. The mean radius of the grains was computed in the cross-sections. (For interpretation of the references to color in this figure legend, the reader is referred to the web version of this article.)

moving box along the direction of the driving force might affect the outcome of simulations. To avoid such errors, we performed several benchmark simulations and found that considering a moving box of 35ℓ (transparent red domain in Fig. 3a) is enough to avoid the effect of non-localities on the front's evolution in our current setup. A direct comparison presented in Fig. 3b shows that the integration of the governing equations within the moving box precisely reproduces the results of the full-domain simulations while reducing the memory consumption and run-time by a factor of three. Obviously, the computational gain achieved by using the moving box increasingly grows with the size of the simulation box and the period of simulations. The scaling behavior of the DGG simulations with regard to the initial number of grains is elaborated in the SM Fig. S3.

For the computation of the average grain size on any plane (bottom boundary of the moving box or in a cross-section) we evaluate the area of each phase-field A_i and define the respective radius as $\sqrt{A_i/\pi}$. The grain size on the evolving front is computed in a similar manner but over the curved surface of the evolving front. For this purpose, we evaluate the volume of the diffuse interface on the evolving front, then scale by the interface width η to obtain the equivalent area of the existing phase-fields.

4. Results

4.1. Full-domain simulations

The full-domain simulation refers to our simulations in $450\ell \times 450\ell \times 205\ell$ domains. These were performed for a range of intensities δg between 1 and 10 MJ m^{-3}, with IGD1 and IGD2 initializations. The growth kinetics are studied in the cross-section perpendicular to the z-axis, i.e., by studying the size of grains in each cross-section and their difference along the z-axis. Since DGG occurs along this axis, the length of grown grains in this direction can be used to redefine the time. Here the simplest assumption can be, to consider a unique relation between time and the evolved microstructure in that direction: This has been the assumption in the experimental evaluation of DGG in

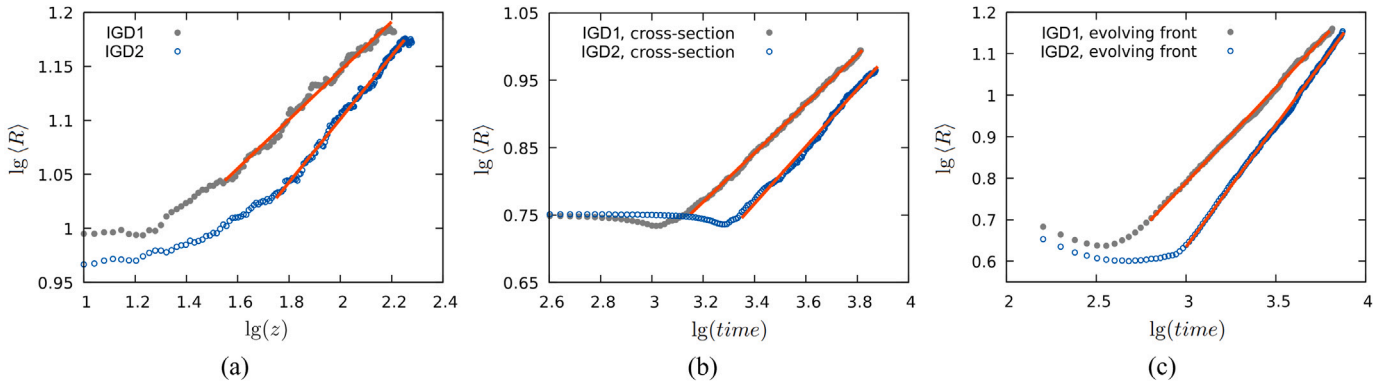

Fig. 5. Evolution of average grain size for the simulation with the energy intensity of 2.4 MJ m^{-3}. (a) Increase of $\langle R\rangle$ across the growth direction. The mean values are computed at the last time increment in the cross-sections $z = const$. The grain growth exponents are 0.23 and 0.29 for IGD1 and IGD2 initializations, respectively. The orange lines show the linear fit performed to gain the power law exponent $\langle R\rangle \sim t^n$. (b) Evolution of $\langle R\rangle$ in the bottom cross-section (boundary), the exponents are 0.36 and 0.42. (c) Finally, the evolution of $\langle R\rangle$ on the evolving front, the exponents are 0.46 and 0.59 respectively. (For interpretation of the references to color in this figure legend, the reader is referred to the web version of this article.)

calcitic prisms [12], where, the growth of calcitic prisms was studied by considering the average size of grains in the cross-sections extracted from microtomography measurements. In such an experimental setup, since temporal information on the microstructure evolution is not available, the length of evolved grains is assumed to be linear in time. During the DGG, however, the grains not only grow along the axis of the driving force but also in any other spatial direction, driven by the local curvature of the grain boundaries, which influences the grain size as well. In simulations, one has the advantage of verifying and analyzing the temporal evolution both along the z-axis as well as within each given cross-section. Fig. 4a depicts selected grains evolved through a simulation, after 7450 time steps. We analyze grain size along the driving force (z-axis) allowing us to investigate the DGG in a quasi-2D setup, in which, the variation in grain size along the z-axis is assumed to represent the temporal evolution of grains. Thus, we obtain the average grain size $\langle R\rangle$ in each cross-section and along the z-axis. Figs. 4b and 4c exemplify two cross-section views at $z_2 > z_1$, demonstrating grain growth in the cross-sections.

Fig. 5a presents the average grain size as a function of height (along z-axis, see Fig. 4), for IGD1 and IGD2 grain initializations. The results show that after a certain initial transient stage, the grain growth accelerates and approaches a steady-state regime. A growth exponent of about 0.29 is obtained over this regime, which is significantly smaller than the normal grain growth's value of 0.5 [38,39]. The results show that the increased randomness of initial grains (IGD1 initialization) only slightly decreases the exponent. The influence of the magnitude of the driving force on the growth exponent is given in the SM, Fig. S4. The size of the simulation domain is however not enough to make a fair comparison. This issue is resolved when using the moving box for our simulations, as discussed in the next section.

Further, we analyzed the growth kinetics (i) on the bottom of the simulation domain (in the cross-section) as well as (ii) directly on the evolving front of growth. These two cases represent the least and the most affected areas by the directional driving force. The results are shown in Figs. 5b and 5c, respectively. Power-law growth with exponents 0.42 and 0.59, for the bottom and front cases, respectively. These values are larger than the exponent corresponding to the analysis along z-axis (0.29) and closer to the normal grain growth exponent. These indicate that although the in-plane evolution is anywhere affected by the directional driving force, evaluation of the grains along z-axis, as discussed above and in [12], might not be fully representative of the DGG and the cross-section analysis along the z-axis and the in-plane growth kinetics must be understood and analyzed as well. In the following, we focus on studying the evolving front which is of the highest practical interest.

4.2. Effect of directional driving force

The dual effects of the directional driving force and curvature-driven grain boundary motion are extremely convoluted. This requires a systematic simulation investigation to reveal the effect of the driving force on the growth kinetics. First, in the proposed modification of mean-field modeling, although Eq. (20) does not explicitly depend on the directional driving force, its effect is captured by modifying the curvature effect through parameter β, see Eq. (1). This modification of the curvature-driven motion manifests through the out-of-plane forces, which then result in a different growth scaling behavior than the normal grain growth, as demonstrated and discussed in the previous section. Using the growth exponent $n = \frac{1}{2+\beta}$, we are able to explore the relationship between the growth kinetics and the applied directional driving force. For this purpose, we systematically studied a series of ten simulations with δg ranging between 1 and 10 MJ m^{-3}, see Fig. 7. Again, both initialization strategies were considered. The moving box method was applied here for computational efficiency and obtaining prolonged simulations.

Fig. 6 shows the results of DGG simulations. After an initial transient stage, a power-law growth is established in all cases. We found that the growth exponent shows a significant dependence on the magnitude of the driving force. The growth kinetics also depend on the initialization but it converges over the longer course of simulation. We, therefore, further our analyses considering only the IGD2 initialization in the following. To make a better comparison, the values of β and n are extracted, based on Eq. (20), and plotted in Fig. 7. We found that the value of β varies between -0.6 and -0.3 with a complex dependence on the driving force. The physical origins behind these behaviors in DGG are discussed in the next section. We also note that the DGG grain size distribution could not converge to a self-similar solution, in contrast to our 3D MPF studies of normal grain growth [39]. This is centrally due to the nature of DGG, in which, the presence of the external driving forces influences the dynamics of the interfaces and results in deviations from a natural curvature-driven motion. Hence, a much larger simulation domain and therefore computational capacity are required to reach a self-similar regime for DGG. Nevertheless, the accumulated distribution of grains' size shows a converging trend, see Fig. S5 in the SM.

5. Discussion

Most microstructures evolve under complex natural or manufacturing processes, needing sophisticated modeling to be investigated. This is becoming increasingly significant due to the recent advances in AM which are intrinsically non-equilibrium processes due to the presence

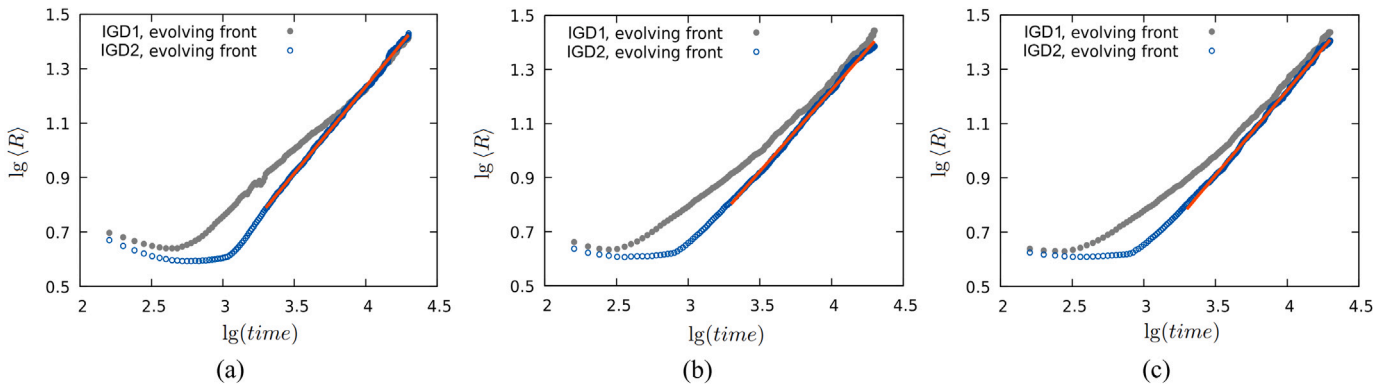

Fig. 6. (a) Evolution of $\langle R \rangle$ on the evolving front at various intensities of the energy field (a) 1.65 MJ m^{-3}, (b) 3.75 MJ m^{-3} and (c) 10 MJ m^{-3}. The orange lines show the linear fit performed to gain the power law exponents. (For interpretation of the references to color in this figure legend, the reader is referred to the web version of this article.)

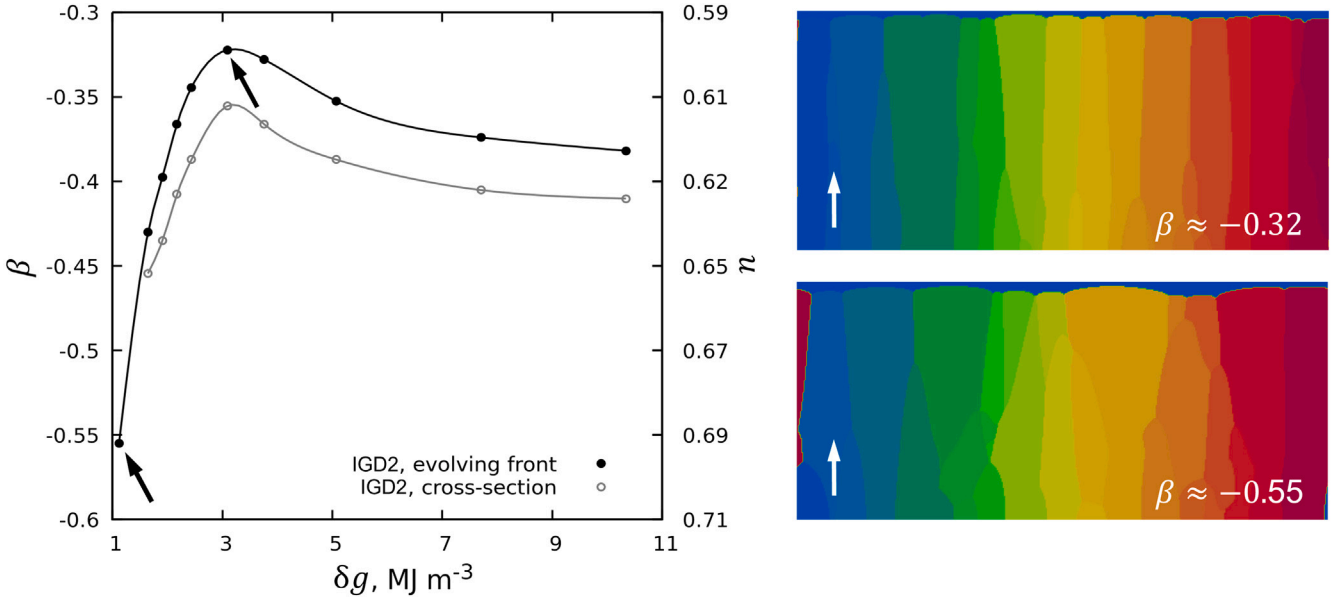

Fig. 7. β values and corresponding growth exponents n in the coarsening law $\langle R \rangle \sim t^n = t^{1/(2+\beta)}$ are shown, determined from the MPF simulations for a range of external forces. The side-view snapshots of the microstructure at the end of two simulations are shown on the right, corresponding to the minimum and maximum β values (marked on the curve).

of dramatic temperature gradients [45,46]. Mesoscale phase-field modeling can play an important role in understanding and determining the processing-microstructure–property relationships in the AM. In this direction, the kinetics of grain growth under a predefined temperature field, i.e., beneath the moving melting pool is of great significance [14, 45,47]. In this work, we combine the strengths of the phase-field simulations with a mean-field modeling to expand the fundamental understanding of DGG under the effect of a directional driving force.

Despite its simple set-up, the current simulations have enabled a systematic consideration of the DGG problem. Foremost, the current results give clear evidence that (i) directional grain growth has a different steady-state power-law kinetics than the normal grain growth, (ii) the exponent in $\langle R \rangle \propto t^n$ for directional driving force cn be obtained from the simulations and (iii) the simulation results can be mapped to the mean-field formulation presented in Section 2.

One essential challenge in studying DGG is the way one can measure the phenomenon. The analysis of the full-domain simulations was performed in three different ways (places in the simulation box), considering

- a fixed cross-section perpendicular to the growth direction, chosen to be $z = 0$ in Figs. 4 and 5b,
- the cross-sections along the growth direction, i.e., $z \neq const$, in Figs. 4 and 5a, and,
- the evolving front, shown in Figs. 3a and 5c.

Typical experimental investigations do not provide access to the evolving front during the DGG, but only the final grain structures, such as in Fig. 4a, resulting from the process. As a result, the analys is of the grains in cross-sections is useful. Along the DGG axis, the cross-sections are thus interpreted as a series of snapshots throughout the DGG process, e.g. considered by [12]. Our results demonstrate however that the first technique significantly underestimates the growth exponents, which means that the association of the z-axis (growth direction) with the time scale is not plausible. The extraction of the growth kinetics from a given microstructure using a mean-field approach is in general incorrect.

The values of β and n for the cross-section and the evolving front are shown in Fig. 7 for comparison. For the smallest driving force, a steady power-law could not be deduced from the cross-section analysis. Nevertheless, we found that apart from the difference in the absolute values, the trends in β (n) are similar to the evolving front, Fig. 7. The systematic deviation is explained as follows.

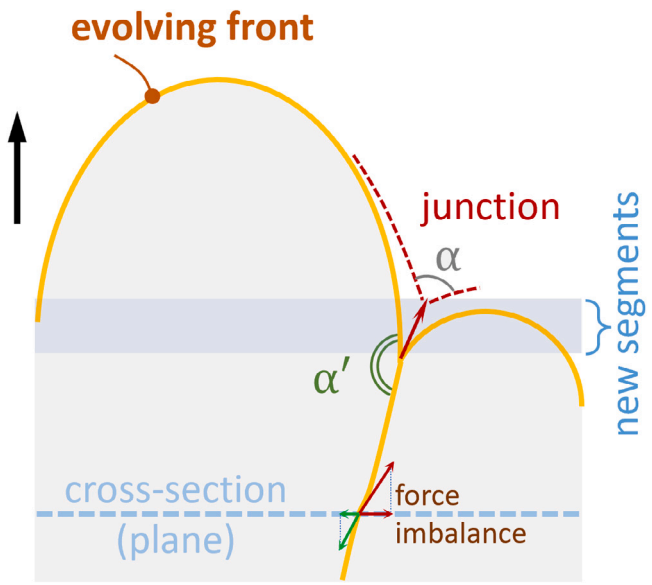

Fig. 8. Schematic sketches of the evolving front and a cross-section across two grains. The force imbalance at the grain boundary junctions (in the direction of the driving force) imposes competitive growth of the grains. Isotropic grain boundary energy is applied, which means that the stable triple junction configuration (plotted in red) tends to angle $\alpha = 120°$. A similar force imbalance works on the cross-sections, wherever the out-of-plane forces do not match. Note that the growth of grains, if considered in the cross-sectional plane, ignores the curvature portion which is considered in the evolving front. (For interpretation of the references to color in this figure legend, the reader is referred to the web version of this article.)

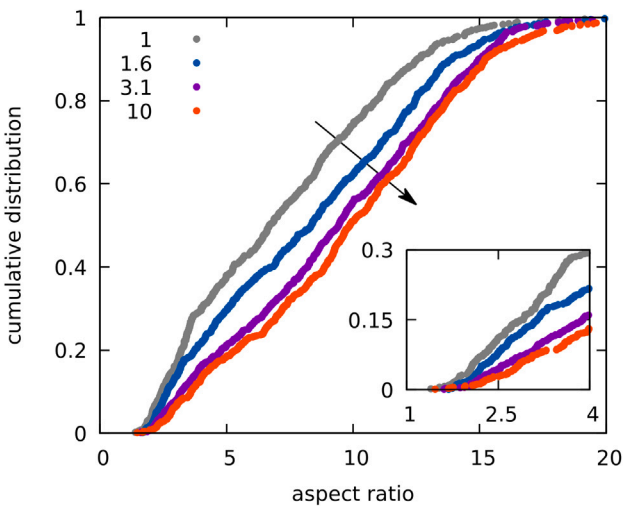

Fig. 9. Cumulative distribution of grains' aspect ratio for various intensities of the driving force field (units MJ m^{-3}). The arrow shows the trend as the driving force increases, indicating the convergence in the distributions. The zoomed inset panel shows the vicinity of small aspect ratios. The simulations were carried out using IGD2 initialization. (For interpretation of the references to color in this figure legend, the reader is referred to the web version of this article.)

For the first two ways of measurements, the consideration of DGG reduces to 2D (cross-sections), in which, the effect of the directional driving force on the grain boundaries comes normal to the plane. In the third case, tracing the grain growth on the evolving front, the curvature contributions of grains are also considered. Note that the evolving front is a quasi-2D surface, not a perfect 2D plane, partially curved due to the force balance required at the grain boundary junctions. Fig. 8 schematically depicts the cross-section and evolving front with the force vectors acting on the grain boundaries. As it is demonstrated, from the cross-section case, we capture the effect of driving force as the imbalance from the forces along the grain boundary junctions. Decomposing this force in the plane, the in-plane components of interfacial tensions affect the in-plane grain growth. For the evolving front, however, we see that the effect of the driving force is in part directly incorporated into the curved grain boundaries, Fig. 8. This indicates that the kinetics of the grain growth on the evolving front is a more complete representative in studying DGG and related parameter β.

The mean-field derivations reveal that the growth rate dramatically changes with β values, Fig. 2a. A lower β value gives a broader, more asymmetric grain size distribution, Fig. 2b. The simulation results show that the β values are negative (the growth exponents are larger than 0.5). We also found that β asymptotically approaches a constant value when increasing the intensity of the driving force, Fig. 7. On the other end of the spectrum, the value of β decreases with decreasing the intensity of the driving forces, and if the driving force is too small, the grains shrink under the dominant effect of their curvature. Most interestingly, we found that for the intermediate values of the driving forces, a maximum value of β (slowest growth kinetics) is achieved.

For a (relatively) large driving force, we found that the driving force tends to make the grain more parallel and thus slows the growth kinetics on the evolving front, resulting in a larger β value. In this case, the newly created segments of the grain boundary tend to orient along the direction of the driving force. In fact, if the driving force is very large, the grains elongate and pack more parallel. This became evident from the distribution of the aspect ratios of the grains, as shown in Fig. 9. We found that with increasing the intensity of the driving force, the grains reach a limiting aspect ratio distribution that imposes the constant value of β (Fig. 7) for very large driving forces.

With decreasing the intensity of the driving force, the grain boundary segments can grow while deviating from the driving force direction. In this case, the curvature-driven grain boundary motion and the equilibrium at the junctions can more effectively influence the evolution of the grains, resulting in a faster growth kinetics (more negative β value) on the evolving front. Grains' morphology compared in the two simulation side views (two different driving forces / β values) in Fig. 7 confirm these findings. Our results show that the cooperation/competition between curvature-induced grain boundary/junction dynamics and the directional driving force can lead to the nonlinear DGG behavior, summarized in Fig. 7.

More complex setups are required to close the gap with real-world scenarios. In particular, besides its intensity, the spatial geometry of the driving force can be an influential factor in DGG. In fact, the interference between the curvature-induced dynamics and the driving force depends on the pattern of the external field. Another factor that can come to play is the nucleation of new grains that can occur along the DGG. These aspects are actually treatable on the basis of the present mean-field and phase-field framework and are suggested for future studies.

6. Conclusions

We investigated the kinetics and mechanisms of DGG using 3D phase-field simulations discussed in the context of a phenomenological extension of the mean-field model for grain growth. We found that in a direction growth procedure, even under a uniform driving force, the growth can be non-linear and thus the association of the time scale with the growth axis can be misleading. An inverse modeling can be suggested, with a model reproducing the temporal evolution of individual grains, like the demonstrated phase-field simulations, which must resemble the observed microstructural changes along the growth axis.

Furthermore, the effects of the intensity of the external driving force and various measurement setups to analyze DGG were systematically studied. The results reveal that a steady-state power-law kinetics can be established in the course of DGG, giving a growth exponent that is

generally larger than 0.5 (normal grain growth). We discuss that the interference between curvature-induced grain boundary dynamics and directional driving force dictates the growth kinetics. The higher the driving force, the higher the growth kinetics, when initially increasing the driving force. Increasing the driving force above a certain threshold, the grain boundary curvature and the force balance at the junctions set the maximum achievable grains' aspect ratio, thus limiting the growth kinetics. The results show that the large-scale phase-field simulations could be reproduced using smaller domains by implementing a moving box setup in the simulations, significantly increasing the total period of DGG which is necessary to reach a steady-state regime. The proposed phenomenological mean-field model and phase-field simulation framework provide a solid ground for investigating DGG in complex processes during additive manufacturing.

CRediT authorship contribution statement

Vitaliy M. Kindrachuk: Methodology, Software, Formal analysis, Writing – original draft. **Reza Darvishi Kamachali:** Conceptualization, Methodology, Software, Writing – review & editing, Supervision.

Declaration of competing interest

The authors declare that they have no known competing financial interests or personal relationships that could have appeared to influence the work reported in this paper.

Data availability

Further data and codes of this study are available per reasonable request.

Acknowledgments

RDK acknowledges financial support from German Research Foundation (DFG) within projects DA 1655/2-1 (Heisenberg program) and DA 1655/3-1.

Appendix A. Supplementary data

Supplementary material related to this article can be found online at https://doi.org/10.1016/j.mtla.2023.101989.

References

[1] Z. Wu, H. Bei, F. Otto, G. Pharr, E. George, Recovery, recrystallization, grain growth and phase stability of a family of FCC-structured multi-component equiatomic solid solution alloys, Intermetallics 46 (2014) 131–140.
[2] M. Dao, L. Lu, R. Asaro, J. De Hosson, E. Ma, Toward a quantitative understanding of mechanical behavior of nanocrystalline metals, Acta Mater. 55 (12) (2007) 4041–4065.
[3] M.H. Frey, D.A. Payne, Grain-size effect on structure and phase transformations for barium titanate, Phys. Rev. B 54 (1996) 3158–3168.
[4] G.L. Messing, S. Trolier-McKinstry, E.M. Sabolsky, C. Duran, S. Kwon, B. Brahmaroutu, P. Park, H. Yilmaz, P.W. Rehrig, K.B. Eitel, E. Suvaci, M. Seabaugh, K.S. Oh, Templated grain growth of textured piezoelectric ceramics, Crit. Rev. Solid State Mater. Sci. 29 (2) (2004) 45–96, http://dx.doi.org/10.1080/10408430490490905.
[5] E. Saiz, L. Gremillard, G. Menendez, P. Miranda, K. Gryn, A. Tomsia, Preparation of porous hydroxyapatite scaffolds, Mater. Sci. Eng.: C 27 (3) (2007) 546–550, Next Generation Biomaterials.
[6] S. Suárez, E. Ramos-Moore, B. Lechthaler, F. Mücklich, Grain growth analysis of multiwalled carbon nanotube-reinforced bulk Ni composites, Carbon 70 (2014) 173–178.
[7] N. Höche, E.O. Walliser, N.J. de Winter, R. Witbaard, B.R. Schöne, Temperature-induced microstructural changes in shells of laboratory-grown arctica islandica (Bivalvia), PLOS ONE 16 (2) (2021) 1–25.
[8] Z. He, J. Ma, C. Wang, Constitutive modeling of the densification and the grain growth of hydroxyapatite ceramics, Biomaterials 26 (14) (2005) 1613–1621.
[9] E. Yang, H. Ho, D.E. Laughlin, J.-G. Zhu, Columnar grain growth of FePt(L1) thin films, J. Appl. Phys. 111 (7) (2012) 07B720, arXiv:https://pubs.aip.org/aip/jap/article-pdf/doi/10.1063/1.3679463/15090918/07b720_1_online.pdf.
[10] D. Zöllner, Treating grain growth in thin films in three dimensions: A simulation study, Comput. Mater. Sci. 125 (2016) 51–60.
[11] Z. Zhang, G. Chen, G. Chen, Dynamics and mechanism of columnar grain growth of pure iron under directional annealing, Acta Mater. 55 (17) (2007) 5988–5998.
[12] B. Bayerlein, P. Zaslansky, Y. Dauphin, A. Rack, P. Fratzl, I. Zlotnikov, Self-similar mesostructure evolution of the growing mollusc shell reminiscent of thermodynamically driven grain growth, Nature Mater. 13 (2014) 1102–1107.
[13] P. Kürnsteiner, P. Bajaj, A. Gupta, M.B. Wilms, A. Weisheit, X. Li, C. Leinenbach, B. Gault, E.A. Jägle, D. Raabe, Control of thermally stable core-shell nano-precipitates in additively manufactured Al-Sc-Zr alloys, Addit. Manuf. 32 (2020) 100910.
[14] M. Yang, L. Wang, W. Yan, Phase-field modeling of grain evolutions in additive manufacturing from nucleation, growth, to coarsening, npj Comput. Mater. 7 (56) (2021) 12.
[15] A.F. Chadwick, P.W. Voorhees, The development of grain structure during additive manufacturing, Acta Mater. 211 (2021) 116862.
[16] T. Xue, Z. Gan, S. Liao, J. Cao, Physics-embedded graph network for accelerating phase-field simulation of microstructure evolution in additive manufacturing, npj Comput. Mater. 8 (201) (2022).
[17] M. Hillert, On the theory of normal and abnormal grain growth, Acta Metall. 13 (3) (1965) 227–238.
[18] L. Brown, A new examination of classical coarsening theory, Acta Metall. 37 (1) (1989) 71–77.
[19] S. Coughlan, M. Fortes, Self-similar size distributions in particle coarsening, Scr. Metall. Mater. 28 (12) (1993) 1471–1476.
[20] P. Rios, Comparison between a computer simulated and an analytical grain size distribution, Scr. Mater. 40 (6) (1999) 665–668.
[21] A.L. Cruz-Fabiano, R.E. Logé, M. Bernacki, Assessment of simplified 2D grain growth models from numerical experiments based on a level set framework, Comput. Mater. Sci. 92 (2014) 305–312.
[22] L. Maire, B. Scholtes, C. Moussa, et al., Improvement of 3D mean field models for capillarity-driven grain growth based on full field simulations, J. Mater. Sci. 51 (2016) 10970–10981.
[23] J. Furstoss, M. Bernacki, C. Ganino, C. Petit, D. Pino-Muñoz, 2D and 3D simulation of grain growth in Olivine aggregates using a full field model based on the level set method, Phys. Earth Planet. Inter. 283 (2018) 98–109.
[24] T. Breithaupt, L.N. Hansen, S. Toppaladoddi, R.F. Katz, The role of grain-environment heterogeneity in normal grain growth: A stochastic approach, Acta Mater. 209 (2021) 116699.
[25] Y. Li, Z. Wang, Y. Wang, J. Li, J. Wang, Revealing curvature and stochastic effects on grain growth: A thermodynamic perspective from extremal principle, Scr. Mater. 217 (2022) 114766.
[26] R. Darvishi Kamachali, C. Schwarze, Inverse ripening and rearrangement of precipitates under chemomechanical coupling, Comput. Mater. Sci. 130 (2017) 292–296.
[27] C. Schwarze, R. Darvishi Kamachali, M. Kühbach, C. Mießen, M. Tegeler, L. Barrales-Mora, I. Steinbach, G. Gottstein, Computationally efficient phase-field simulation studies using RVE sampling and statistical analysis, Comput. Mater. Sci. 147 (2018) 204–216.
[28] R. Darvishi Kamachali, E. Borukhovich, N. Hatcher, I. Steinbach, DFT-supported phase-field study on the effect of mechanically driven fluxes in Ni4Ti3 precipitation, Modelling Simul. Mater. Sci. Eng. 22 (2014) 034003.
[29] J. Park, R. Darvishi Kamachali, S.-D. Kim, S.-H. Kim, C.-S. Oh, C. Schwarze, I. Steinbach, First evidence for mechanism of inverse ripening from in-situ TEM and phase-field study of δ' precipitation in an Al-Li alloy, Sci. Rep. 9 (2019) 3981.
[30] R. Darvishi Kamachali, C. Schwarze, M. Lin, M. Diehl, P. Shanthraj, U. Prahl, I. Steinbach, D. Raabe, Numerical benchmark of phase-field simulations with elastic strains: Precipitation in the presence of chemo-mechanical coupling, Comput. Mater. Sci. 155 (2018) 541–553.
[31] R. Darvishi Kamachali, S.-J. Kim, I. Steinbach, Texture evolution in deformed AZ31 magnesium sheets: Experiments and phase-field study, Comput. Mater. Sci. 104 (2015) 193–199.
[32] D.-U. Kim, P.-R. Cha, S.G. Kim, W.T. Kim, J. Cho, H.-N. Han, H.-J. Lee, J. Kim, Effect of micro-elasticity on grain growth and texture evolution: A phase field grain growth simulation, Comput. Mater. Sci. 56 (2012) 58–68.
[33] R. Schiedung, R. Darvishi Kamachali, I. Steinbach, F. Varnik, Multi-phase-field model for surface and phase-boundary diffusion, Phys. Rev. E 96 (1) (2017) 012801.
[34] C. Ma, M. Zhao, T. Xin, L. Wu, R. Pan, J. Qin, J. Zhang, Phase-field simulation of grain nucleation, growth, and Rayleigh distribution of U3Si2 nuclear fuel, Front. Energy Res. 10 (2023).
[35] R. Laskowski, R. Ahluwalia, G.T.W. Hock, C.S. Ying, C.-N. Sun, P. Wang, D.T.C. Cheh, N.M.L. Sharon, G. Vastola, Y.-W. Zhang, Concurrent modeling of porosity and microstructure in multilayer three-dimensional simulations of powder-bed fusion additive manufacturing of inconel 718, Addit. Manuf. 60 (2022) 103266.

[36] T. Pusztai, L. Rátkai, L. Horváth, L. Gránásy, Phase-field modelling of directional melting of lamellar and rod eutectic structures, Acta Mater. 227 (2022) 117678.
[37] R. Darvishi Kamachali, Grain Boundary Motion in Polycrystalline Materials (Ph.D. thesis), Univ.-Bibliothek, 2013.
[38] R. Darvishi Kamachali, I. Steinbach, 3-D phase-field simulation of grain growth: Topological analysis versus mean-field approximations, Acta Mater. 60 (6–7) (2012) 2719–2728.
[39] R. Darvishi Kamachali, A. Abbondandolo, K.F. Siburg, I. Steinbach, Geometrical grounds of mean field solutions for normal grain growth, Acta Mater. 90 (2015) 252–258.
[40] K. Wu, J. Jeppsson, P. Mason, Mean field modeling of grain growth and Zener pinning, J. Phase Equilib. Diffus. 43 (2022) 866–875.
[41] I.M. Lifshitz, V.V. Slyozov, The kinetics of precipitation from supersaturated solid solutions, J. Phys. Chem. Solids 19 (1) (1961) 35–50.
[42] I. Steinbach, Phase-field models in materials science, Model. Simul. Mater. Sci. Eng. 17 (2009) 073001.
[43] M. Tegeler, O. Shchyglo, R. Darvishi Kamachali, A. Monas, I. Steinbach, G. Sutmann, Parallel multiphase field simulations with OpenPhase, Comput. Phys. Comm. 215 (2017) 173–187.
[44] W. Boettinger, F. Emeritus, The solidification of multicomponent alloys, J. Phase Equilib. Diffus. 37 (2016) 4–18.
[45] Y. Ji, L. Chen, L.-Q. Chen, Understanding microstructure evolution during additive manufacturing of metallic alloys using phase-field modeling, in: Thermo-Mechanical Modeling of Additive Manufacturing, Elsevier, 2018, pp. 93–116.
[46] T. Keller, G. Lindwall, S. Ghosh, L. Ma, B.M. Lane, F. Zhang, U.R. Kattner, E.A. Lass, J.C. Heigel, Y. Idell, et al., Application of finite element, phase-field, and CALPHAD-based methods to additive manufacturing of Ni-based superalloys, Acta Mater. 139 (2017) 244–253.
[47] T. Takaki, S. Sakane, M. Ohno, Y. Shibuta, T. Aoki, C.-A. Gandin, Competitive grain growth during directional solidification of a polycrystalline binary alloy: Three-dimensional large-scale phase-field study, Materialia 1 (2018) 104–113.